3.3 Synchrotron Radiation Instrumentation Engineering

The Experimental Facilities Division develops instrumentation, beamline components, and front-end components, for SRI CAT, for other CATs, and for the APS facility. In addition, engineering support is provided to APS users and to the APS Operations Division.

3.3.1 Undulator-Only Front End

The original design of the ID beamline front ends was based on compatibility with various undulators and wigglers. These front ends are standardized and modularized to reduce the cost and engineering effort. They are easy to install and are reliable (Shu and Kuzay, 1994). However, since the standard APS ID, undulator A, achieved excellent performance in generating high-intensity x-ray radiation in the spectral range of 3.2 to 45 keV by using the first, third, and fifth harmonics of radiation, a great majority of the APS users have chosen an undulator as the only source for their ID beamline. Compared with a wiggler source, the undulator source has a much smaller horizontal divergence, providing an opportunity to optimize the beamline front-end design to a new level.

The front end designed for beamline 32-ID is the prototype for a new undulator-only beamline (Shu et al., 2000a). It is called the version 1.5 undulator-only front end. The major design change between the new front end and the original is the optical apertures of the front-end fixed masks. Smaller horizontal optical apertures on the fixed masks allowed us to design the V-shaped compact photon shutter P2-30 shown in Fig. 3.13. This new photon shutter is made from GlidCop™ and stainless steel using the APS-developed box-type explosive bonding technique (Shu et al., 2000b). Compared with the original P1-20 photon shutter, P2-30 provides 150% thermal loading capacity with more than 50% manufacturing cost savings. Figure 3.14 shows the internal water-cooling surfaces and the explosive bonding structure. Table 3.2 shows a comparison of the aperture parameters between the new front end and the original one.

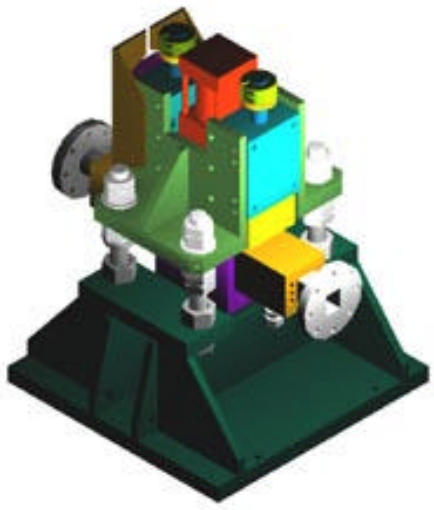

Fig. 3.13. V-shaped compact photon shutter P2-30.

During the past year, the 32-ID front end has been fully commissioned and is now operational. The construction of three more undulator-only v.1.5 front ends is in progress. Figure 3.15 is a schematic layout of the 32-ID beamline front end.

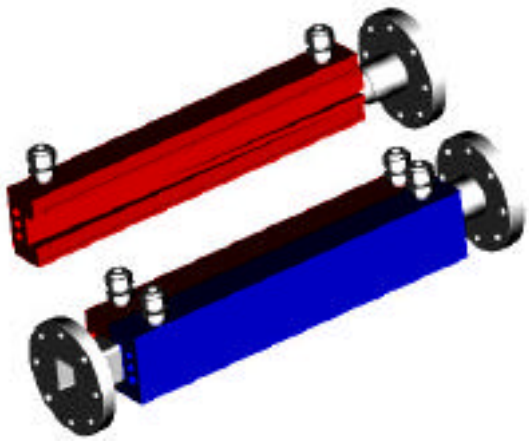

Fig. 3.14. Internal water-cooling surfaces and the explosively bonded structure of the photon shutter P2-30.

3.3.2 Double-Undulator Split Beamlines

The dogleg bend between the sector 4 undulator beamlines is also of interest to other APS CATs. We have examined several preliminary designs for new straight sections and front ends with double-undulator configurations:

- 13.0-mrad dogleg double undulator
- 1.0-mrad dogleg double undulator
- 0.3-mrad dogleg double undulator
- 5-meter undulator

The design for the large-angle 13.0-mrad dogleg double-undulator configuration requires two independent front ends with independent vacuum control for each undulator branch and considerable redesign of storage ring vacuum components. Limited by maintenance space in the storage ring tunnel, these two front ends would need to share supporting systems and specially designed twin photon shutters.

Table 3.2 Comparison of the front-end design parameters.

Aperture parameters		Original front end	New undulator front end
Pre-fixed mask optical aperture	(input)	N/A	38 mm (H) x 26 mm (V)
	(output)	N/A	20 mm (H) x 12 mm (V)
1st fixed mask optical aperture	(input)	38 mm (H) x 26 mm (V)	24 mm (H) x 16 mm (V)
	(output)	24 mm (H) x 12 mm (V)	11 mm (H) x 6 mm (V)
1st photon shutter coverage		70 mm (H) x 16 mm (V)	20 mm (H) x 20 mm (V)
Lead collimator(optical aperture)		62 mm (H) x 20 mm (V)	32 mm (H) x 20 mm (V)
(shielding aperture)		68 mm (H) x 26 mm (V)	38 mm (H) x 26 mm (V)
Fast valve			70 mm (H) x 18 mm (V)
2nd fixed mask optical aperture	(input)	66 mm (H) x 18 mm (V)	21.5 mm (H) x 14 mm (V)
	(output)	54 mm (H) x 6 mm (V)	12.7 mm (H) x 5.2 mm (V)
2nd photon shutter coverage		70 mm (H) x 10 mm (V)	20 mm (H) x 20 mm (V)
Wall collimator (optical aperture)		72 mm (H) x 20 mm (V)	32 mm (H) x 20 mm (V)
(shielding aperture)		78 mm (H) x 26 mm (V)	38 mm (H) x 26 mm (V)
Exit fixed mask (input)		40 mm (H) x 12 mm (V)	21 mm (H) x 11 mm (V)
(output)		4.5 mm (H) x 4.5 mm (V)	3 mm (H) x 2 mm (V)
Exit Be-window		5 mm (H) x 5 mm (V)	3.6 mm (H) x 2.6 mm (V)

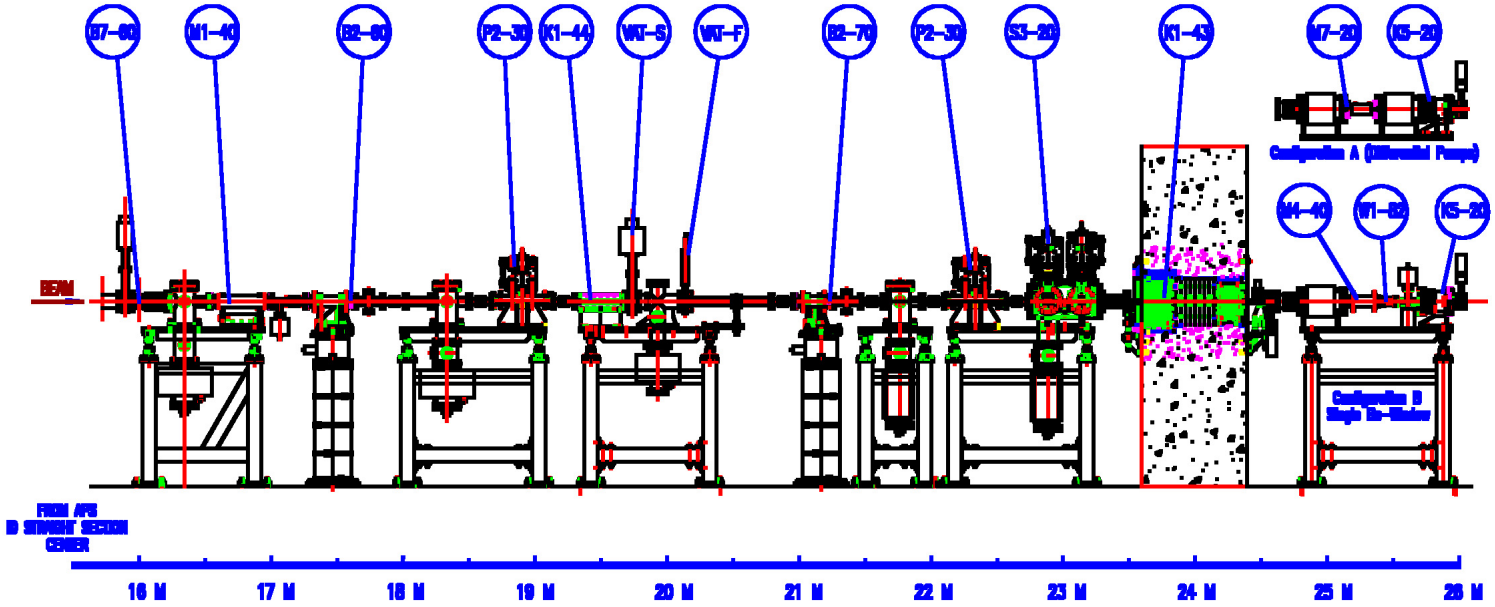

Fig. 3.15. Schematic layout of the 32-ID beamline front end. Beam enters from the left and travels to the right. B7-*60: BM mask, M1-40: ID mask, B2-60: first XBPM/mask, P2-30: first photon shutter, K1-44: collimator, VAT-S: UHV valve, VAT-F: fast valve, B2-70: second XBPM/mask, P2-30: second photon shutter, S3-20: safety shutter, M4-40: exit mask for Be-window, W1-82: single Be-window, K5-20: in-vacuum collimator, M7-20: exit mask for differential pumps.*

For the 0.3-mrad dogleg double-undulator configuration, a single shared front end is a better solution. The SRI-CAT 4-ID front end is an example of such a shared front end, having a 0.27-mrad dogleg separation. We have analyzed the thermal load on the second photon shutter with 0.3-mrad dogleg double-undulator A configuration.

As shown in Fig. 3.16, the peak power density at the front-end second photon shutter in this configuration is 30% higher than the peak power density in the single 2.4-m undulator A case due to the overlap of the two beams. Figure 3.17 shows a finite element analysis result of the maximum surface temperature on the original second photon shutter with this new thermal load. To control the surface temperature, we would need to design a set of new fixed masks with smaller optical apertures for this configuration and reduce the second photon shutter glancing incidence angle from 2 degrees to 1.5 degrees. The x-ray fans from each undulator are separated on the first photon shutter in the 1.0-mrad dogleg configuration, reducing the power density on the shutter. Based on user interest and the feasibility studies, a 1.0-mrad beamline separation has been selected as the most practical.

With the same technical approach, we can upgrade existing undulator/wiggler front ends to be compatible with a 5-meter undulator configuration. More experimental studies at the SRI-CAT 4-ID test facility will help us to optimize the final design.

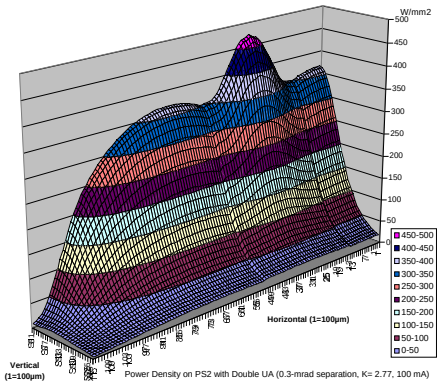

Fig. 3.16. Peak power density at the front-end second photon shutter location in the 0.3-mrad dogleg double-undulator configuration.

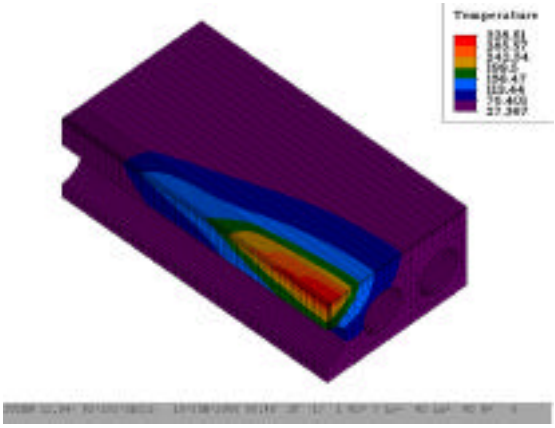

Fig. 3.17. A finite element analysis result of the maximum surface temperature on the original second photon shutter with the thermal load with the 0.3-mrad dogleg double-undulator configuration.

3.3.3 Impact Studies on the Bending Magnet Front Ends for a 6-mm Lattice Offset

At the APS, beam stability and orbit control at the micron level have been design requirements. For both the electron beam and the x-ray beam significant effort has been expended to achieve this (Decker and Singh, 1999; Shu et al., 1997). Decker and Singh summarize the current position on these developments and make several proposals to achieve precise closed-loop local feedback. With the proposed schemes, the well-demonstrated interference of the x-ray beam position monitor (XBPM) signals by the bending magnet (BM) radiation and the corrector and steering magnets will be, for the most part, eliminated.

The primary proposal is to move the upstream and downstream dipole magnets in two consecutive sectors on the APS lattice by 6 mm inboard leaving the IDs untouched. We have studied the potential impact of the lattice offset would be on the APS BM front ends. This impact was investigated by comparing the bremsstrahlung and the synchrotron-radiation ray tracings in regards to the beam missteering with or without the offset alignment implementation in the front ends. Figure 3.18 is a synchrotron radiation ray tracing in the BM front end with the fixed masks realigned. As shown in Fig. 3.18, the BM source is displaced by 6.364 mm inboard. The three fixed masks will be displaced in the horizontal plane by 3.621, 2.278 and 0.846 mm so that they end up on the new beam centerline, which then defines an improved offset angle of 0.298 mrad compared to an unaligned front-end configuration with an offset angle of

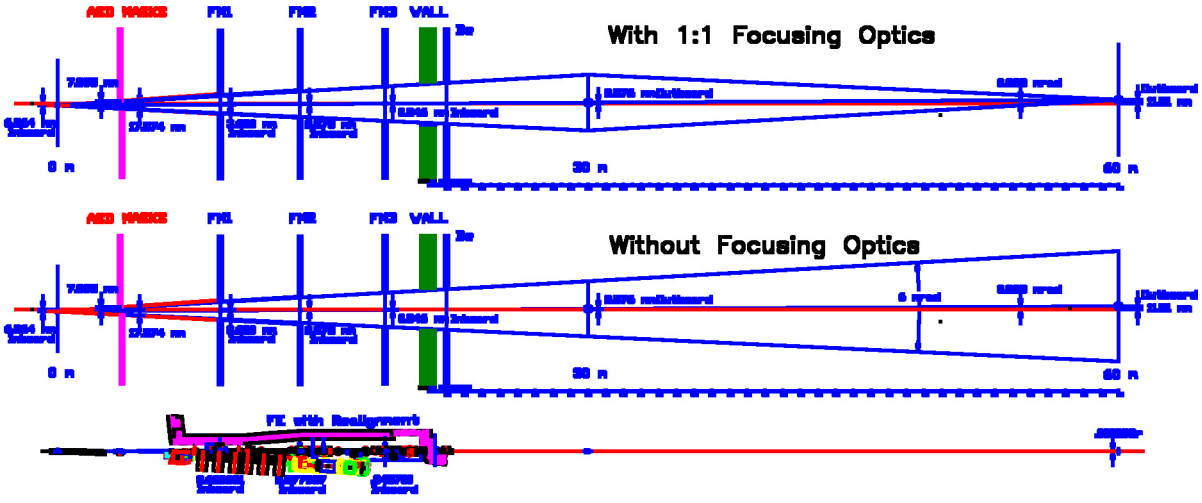

Fig. 3.18. Synchrotron radiation ray tracing in the BM front end with fixed masks realigned for the lattice offset.

0.376 mrad. With the realignment, the BM radiation horizontal fan will be preserved at 6 mrad normal value.

An examination of the bremsstrahlung ray tracings shows no impact as far as the bremsstrahlung is concerned.

3.3.4 Beamline Components Development

3.3.4.1 New XBPM development

Smaller optical apertures on the fixed masks in the new front end create new technical challenges for the XBPM design. To solve the problems experienced during the 32-ID commissioning process, a new compact photoemission-type chemical-vapor-deposition (CVD)-diamond XBPM has been designed (Fig. 3.19) and was tested on the 32-ID front end.

A new XBPM that uses shadowed BM radiation has been proposed for the dogleg double-undulator configurations. Preliminary tests of this new BM-radiation-based XBPM are in progress.

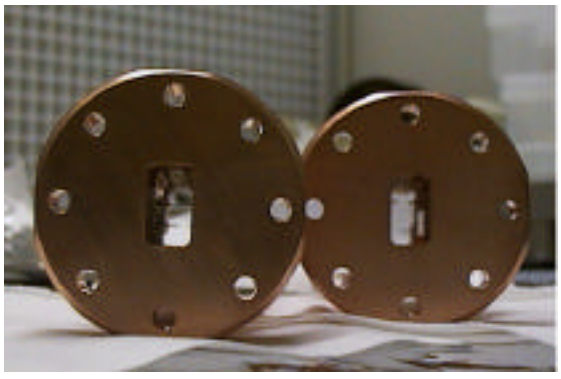

Fig. 3.19. A new compact photoemission-type CVD-diamond XBPM for the 32-ID front end.

3.3.4.2 Wide-angle monochromatic photon shutter

A special wide-horizontal-angle monochromatic photon shutter was designed for the IMM-CAT 8-ID troika-type hard-x-ray multiple-branched beamline. The shutter will be used to regulate the beam reflected from the diamond single-bounce ESRF monochromator in the 8-ID-D hutch. When closed, the shutter must completely prevent the monochromatic beam and any associated stray radiation from entering the 8-ID-E station. When open, the shutter will permit reflected radiation over a range of two-theta from 15 to 50 degrees.

3.3.4.3 Technology development for white-beam components

Beamline components test facility at 4-ID

The SRI-CAT 4-ID-A station houses a vacuum chamber immediately following the front-end differential pump for the testing of new front-end and beamline components. It is called the beamline components test facility (BCTF). This vacuum chamber is equipped with large access flanges for the testing components. Numerous smaller flanges are used for thermocouple, electrical and water-cooling feedthroughs. An infrared mirror is mounted inside the chamber, so that an infrared camera is able to image the temperature distribution on the internal thermal-loading surface of the testing devices as shown in Fig. 3.20. A motorized table is used for varying the angle of incidence on the component under test. The BCTF started commissioning activity in April 2000.

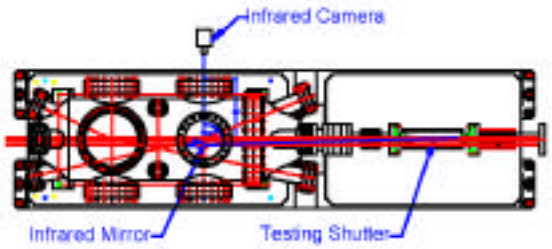

Fig. 3.20. BCTF with infrared mirror and camera.

Recent beamline experiments using infrared thermal imaging

Several experiments have been performed on various beamline components. Typically, thermal images are obtained by viewing through a sapphire window into a vacuum chamber where the component strike surface is located. Often, due to physical constraints, images must be viewed off highly reflective gold infrared mirrors designed to allow a line of sight down the beamline to the target of interest.

Several experiments were conducted at 1-ID-B using a variety of filter materials. The goal was to characterize the maximum operating temperatures of various filter materials commonly used in beamlines. This information can be used to determine maximum allowable operating conditions. Figure 3.21 shows the results of various filter materials of different thicknesses, including graphite, aluminum, diamond, and copper. The full open beam was allowed to strike the filter materials at various undulator gap positions. Note that the maximum surface temperature does not necessarily occur at closed-gap conditions, because the wavelength distribution of the beam changes as a function of undulator gap.

Another set of experiments was performed at 1-ID-A to assess the performance of the new B2-20 beam position monitor under both single- and double-undulator operation modes. Figure 3.22 shows the maximum surface temperature versus undulator gap for both double- and single-undulator configurations. With double-undulator operation, the upstream first undulator is in the closed-gap 11-mm position throughout the tests. Results agree well with predicted operating temperatures.

The new P4-39 white beam photon shutter was recently tested at 4-ID-A with excellent results. Figure 3.23 shows the maximum surface temperature versus undulator gap down to the closed-gap position. Although the ring current was only 75 mA during the test run, the extrapolated results at maximum ring current agree with analytically predicted values.

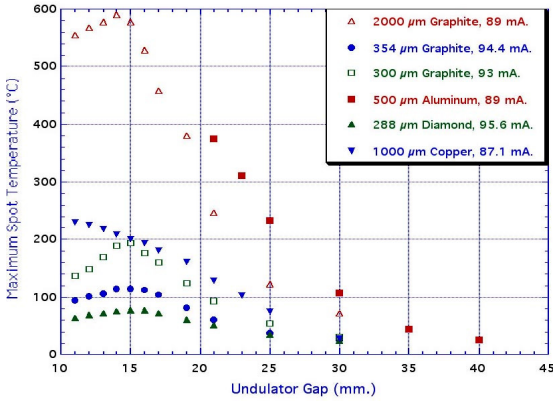

Fig. 3.21. Filter experiments at 1-D-B. Various filter materials of different thicknesses were exposed to the full open beam at various undulator gap positions. There were 250 µm and 300 µm Be windows upstream.

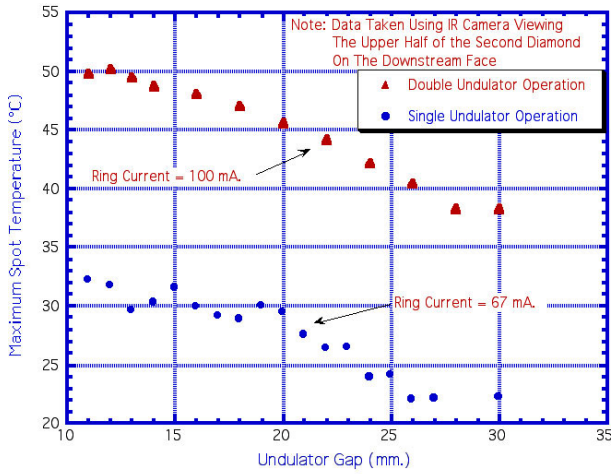

Fig. 3.22. B2-20 beam position monitor tests. Data taken at 1-ID-A with double- and single-undulator operation.

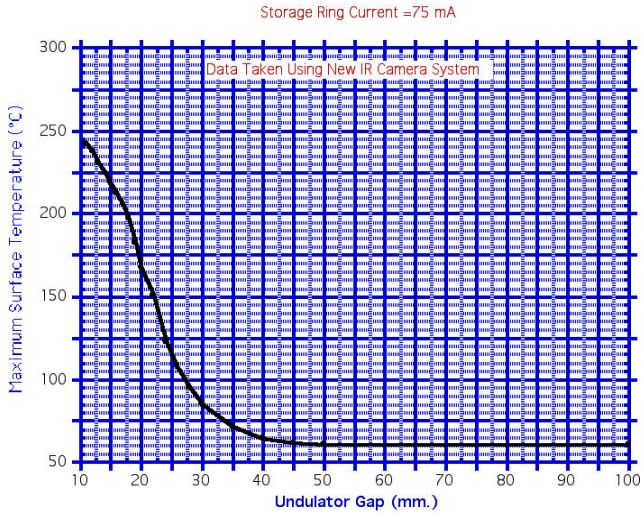

Fig. 3.23. P4-39 white-beam photon-shutter test at the 4-ID-A BCTF. Storage-ring current was 75 mA.

Erosion/corrosion of machinable tungsten in water

As a result of a beamline mishap with a water-cooled tungsten slit, we discovered that significant erosion/corrosion occurs with machinable tungsten when exposed to water. Figure 3.24 shows a cut-away section of a tungsten slit, the water passages are

Fig. 3.24. Cut-away section of a tungsten slit, showing the corroded water passages.

severely corroded from the water used to cool the slit.

Machinable tungsten consists of 95% tungsten, 3.5% nickel and 1.5% iron and is manufactured using a powder metallurgy process. The nickel and iron are used to bind the matrix together, forming a very strong yet machinable material. Oxygen present in water reacts with the iron in the matrix forming iron oxide. The brittle iron oxide then erodes away locally leaving the machinable tungsten without a binding matrix. As this occurs, the tungsten particles erode away from the material without the matrix to keep them bound in place. Once the erosion/corrosion process begins, it progressively accelerates as more and more surface area is exposed to the water.

Four samples were tested for a period of one year; two of the samples were nickel coated and the other two samples were uncoated. Each sample was subjected to 1 gpm of continuous water flow, and the samples were periodically removed and weighed. The weight loss of the samples over time was recorded. Figure 3.25 shows the results of the uncoated machinable tungsten

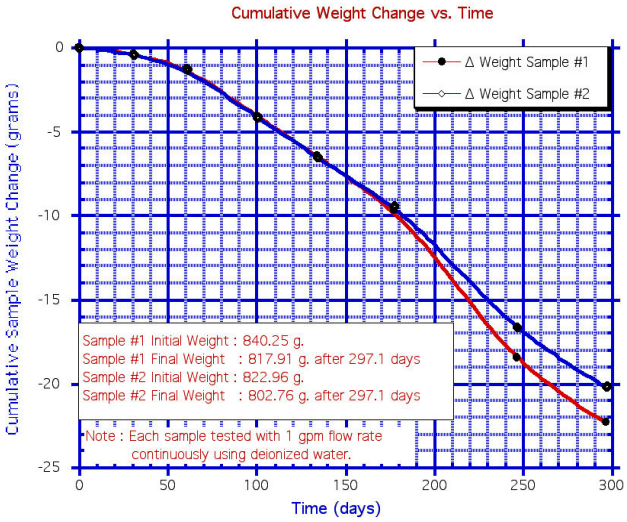

Fig. 3.25. Tests of uncoated machinable tungsten samples exposed to 1 gpm of continuous water flow. Samples were periodically removed and weighed.

samples. Significant weight loss occurred over a very short period, and the weight loss accelerated as more and more material was eroded away. Initially, the nickel coating seemed to reduce the erosion/corrosion rate; however, after a period of time, the nickel was worn away, and the erosion rate increased to the level of the uncoated samples.

It seems that the long-term solution to the erosion/corrosion problem is to remove the oxygen from the water. This prevents iron oxide from being formed, thus corrosion and subsequent erosion can not begin without the oxidation mechanism in place. A better solution for new components made of machinable tungsten is to design them in such a way as to prevent water from ever coming into contact with the tungsten surface. This is the design for the new L5-92 tungsten slits, the cooling water flows through copper tubes that are brazed into the tungsten body.

Explosive bonding

Explosive bonding technology uses the controlled energy of a detonating explosive to create a metallurgical bond between two or more similar or dissimilar metals. It has been extensively used in making the APS high-heat-load beamline and front-end components. In recent years, special explosive bonding units with rectangular joints (box-type) geometries were developed for the APS new high-heat-load beamline components. Based on this new technique, the box form of the component could be built in two halves first, then welded together as shown in Fig. 3.26. Therefore, beamline designers have more freedom to optimize the cooling surface geometry.

Five different high-heat-load beamline components have been designed using this new technique. These include: two white beam photon shutters for beamline integral shutters at 32-ID and 4-ID, a white-beam collimator for 3-ID x-ray collimating lens, a white-beam splitter at 4-ID-A (Fig. 3.26), and an upgraded white-beam grazing-incidence knife-edge slit for 2-ID, shown in Fig. 3.27.

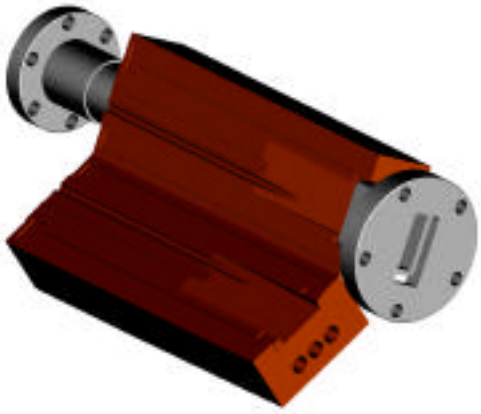

Fig. 3.26. White-beam splitter at 4-ID-A.

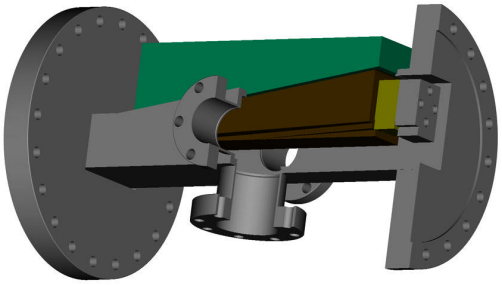

Fig. 3.27. Upgraded white-beam grazing-incidence knife-edge slit for 2-ID.

3.3.4.4 High-resolution and precision instrumentation

Mechanism for artificial channel-cut crystal

We have developed a novel high-stiffness weak-link mechanism having the precision and stability to allow us to align or adjust an assembly of crystals to achieve the same performance as does a single channel-cut crystal. We call it an "artificial channel-cut crystal." Using this mechanism, we can make an outer channel-cut crystal large enough to optimize the nested monochromator's performance and compensate the crystal local temperature and strain variations. This new technique presents a significant opportunity to support the instrumentation development for a high-resolution hard x-ray monochromator with meV energy resolution at the SRI-CAT 3-ID beamline.

Figure 3.28 shows the design of the miniature multiaxis driving structure for the artificial channel-cut crystal. The structure consists of three subassemblies: one base weak-link mechanism and two crystal holders.

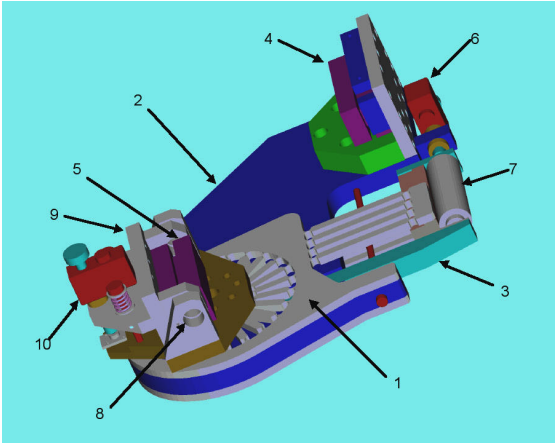

Fig. 3.28. The base mechanism includes a compact sine-bar driving structure for the crystal pitch alignment, which is the key component of the mechanism. There are two groups of stacked thin metal weak-link structures (1) mounted on each side of the base plate (2). A sine-bar (3) is installed on the center of the planar rotary shaft for the pitch alignment between the two (4 4 0) single crystals (4, 5). Two linear drivers are mounted on the base plate serially to drive the sine-bar. The rough adjustment is performed by a Picomotor™ (6) with a 20-nm to 30-nm step size. A Queensgate™ closed-loop controlled PZT (7) with capacitance sensor provides 1-nm resolution for the pitch fine alignment.

To optimize the system stiffness, we have chosen overconstrained mechanisms in this design. The precision of modern photo-chemical machining processes using lithography techniques makes it possible to construct a strain-free (or strain-limited) overconstrained mechanism on a thin metal sheet. By stacking these thin-metal weak-link sheets with align-pins, we can construct a solid complex weak-link structure for a reasonable cost.

A pair of commercial flexure bearings is mounted on one of the crystal holders, and a

Picomotor™-driven structure provides the roll alignment for the crystal.

We have tested the sensitivity of the weak-link sine-bar structure with a laser Doppler angular encoder. A 200-mm-long aluminum arm is mounted on the center of the planar rotary shaft, perpendicular to the sine-bar. A set of prisms is mounted at the end of the arm as a multireflection displacement sensor. During this test, a series of 5-nm incremental steps was applied to the sine-bar by a Queensgate piezoelectric transducer (PZT). The average angular step size measured by the laser Doppler angular encoder is 33 nrad with a 7 nrad rms deviation, which meets the design specification of the weak-link mechanism.

We have tested the first prototype artificial channel-cut crystal as an outer crystal for a 4-bounce high-resolution monochromator with nested configuration at the APS 3-ID-B experiment station. The outer crystals of the monochromator are asymmetrically cut silicon (4 4 0), and the inner channel-cut crystal is silicon (15 11 3). This combination yields a bandpass of 1 meV at 21.6 keV. The monochromator is turnable between 21.5 - 21.7 keV. As a typical case, Fig. 3.29 shows a forty-minute stability result with a 1-meV bandwidth monochromatic beam. The change in transmitted intensity reflects the change in beam position, thermal changes, and crystal angle variations combined. At this point we have not isolated the contribution of the artificial channel-cut crystal assembly alone. However, we infer that the contribution of the angular drift of two crystals attached to each other with the mechanism described here is less than 25 nrad per hour.

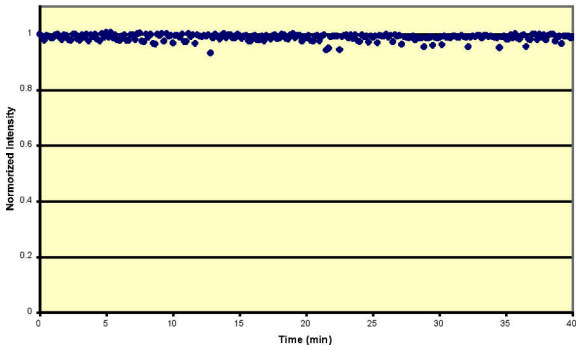

Fig. 3.29. Forty-minute stability result with a 1–meV bandwidth monochromatic beam.

X-ray mirrors for the polarized x-ray facility

The emerging facilities in sector 4 of SRI CAT will provide linearly and circularly polarized x-rays in the intermediate (0.5 to 3 keV) and hard (3-100 keV) x-ray ranges. Intermediate-energy x-rays are created by a novel electromagnetic circularly polarized undulator capable of producing switchable circular and linear polarization, while polarized hard x-rays are formed using a linear undulator with diamond phase-retarding optics. One of the unique features of this sector is the canting of the undulators in the straight section to allow the spatial separation of hard and intermediate x-rays into two separate beamlines that can operate simultaneously.

This separation is made possible with the use of two horizontally deflecting mirrors. The angular adjustments for the beam path require extremely precise rotational motions, with a resolution of 0.15 μrad. For these motions, large-diameter precision ball bearings are chosen over axial bearings. Large open-frame linear stages accomplish the task of moving the mirrors transverse to the beam. These stages allow a compact and symmetrical design.

Rhodium, platinum and multilayer coatings along the water-cooled mirror body enable operations at different energy levels. To move the beam to the individual coatings, each mirror travels a total of 30 mm vertically. All required motions, transverse, vertical, and rotational are applied externally. For optimum performance and ease of maintenance, the mirrors are mounted to large horizontal conflat flanges and covered with bell jar chambers.